ISBN: 978-3-95450-230-1 ISSN: 2673-5350 doi:10.18429/JACoW-IBIC2021-TUOA01

SINGLE-CRYSTAL DIAMOND PIXELATED RADIATION DETECTOR WITH BURIED GRAPHITIC ELECTRODES

C. Bloomer*[1], L. Bobb, Diamond Light Source Ltd, Didcot, UK
M. E. Newton, University of Warwick, Coventry, UK
[1]also at University of Warwick, Coventry, UK

Abstract

A new type of transmissive pixel detector has been developed for synchrotron radiation diagnostics at Diamond Light Source. A thin single-crystal CVD diamond plate is used as the detector material, and a pulsed-laser technique has been used to write conductive graphitic electrodes inside the diamond plate. Instead of using traditional electrodes formed from a layer of surface metallisation, the graphitic electrodes are buried under the surface of the diamond and result in an all-carbon imaging detector. Within the instrument's transmissive aperture there are no surface structures that could be damaged by exposure to radiation beams, and no surface metallization that could introduce unwanted absorption edges. The instrument has successfully been used to image the X-ray beam profile and measure the beam position to sub-micron accuracy at 100 FPS at Diamond Light Source. A novel modulation lock-in technique is used to read out all pixels simultaneously. Presented in this work are measurements of the detector's beam position resolution and intensity resolution. Initial measurements of the instrument's spread-function are also presented. Numerical simulations are used to identify potential improvements to the electrode geometry to improve the spatial resolution of similar future detectors. The instrument has applications in both synchrotron radiation instrumentation, where real-time monitoring of the beam profile is useful for beam diagnostics and fault-finding, and particle tracking at colliders, where the electrode geometries that buried graphitic tracks can provide increased the charge collection efficiency of the detector.

INTRODUCTION

Synchrotron light sources are particle accelerators which are used to generate highly intense beams of UV and X-ray light. At modern synchrotrons monochromatic photon beams of up to 1×10^{14} photons/s and of energies from a few 10 eV up to 100 keV are used to examine a range of biological, chemical, and physical samples. The light produced can be focused down to sub-micron spot sizes [1]. Experimental timescales range from picoseconds, up to years [2, 3].

Common to all the experiments conducted at synchrotrons globally is the requirement to monitor and maintain the stability of the photon beam incident upon the sample: in spatial position, in beam profile, in intensity, in photon energy; and to do so over the range of timescales utilised by the synchrotron users. The typically required photon beam stability at a 3rd generation synchrotron is < 10 % of the beam size, < 1 % of beam intensity, over kHz timescales [4, 5]. New 4th generation synchrotrons have even stricter stability requirements [6]. To provide this level of beam stability, the measurements of the incident photon beam must correspondingly be at least as accurate as these stringent requirements. It is also required that the instruments used to make beam stability measurements are minimally invasive, and mostly transparent to the incident light: a diagnostic instrument that makes a perfect measurement of the beam but does not transmit any of the incident photons through to the sample would not be acceptable! If measurements of the photon beam can be obtained then real-time optics adjustments can be made to keep the beam position stabilised at the sample, and to keep the X-ray intensity maximised.

Non-destructive X-ray beam profile monitoring is essential as synchtrotron and XFEL beamlines increasingly aim to deliver sub-micron beam sizes at their samples points. Significant effort is put into ensuring that precision optics can meet these requirements, from ex-situ measurement and optimisation [7], to in-situ beam profile monitoring and adaptive improvement [8]. It is increasingly common to consider real-time feedback and adaptive optics to ensure that the mirror performance is maintained [9]. The ability to reliably and non-destructively monitor the beam profile is an essential step in ensuring the reliability of the beamline optics.

DIAMOND DETECTORS

To fulfil these requirements for non-destructive monitoring, single crystal chemical vapour deposition (scCVD) diamond makes for an excellent non-invasive detector material: a 50 µm plate is mostly transparent to > 4 keV photons, radiation tolerant, and exhibits good detector properties. The

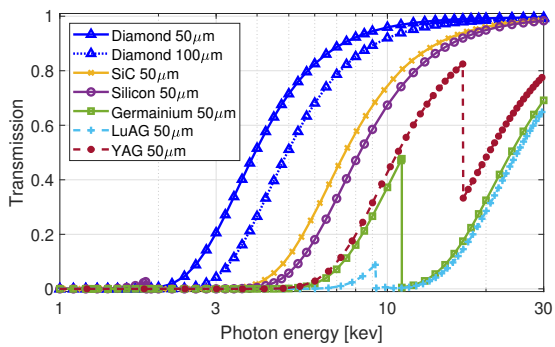

Figure 1: The X-ray transmissivity of scCVD diamond alongside other common solid-state detector materials for ionizing radiation, and common fluorescent materials.

* chris.bloomer@diamond.ac.uk

ISBN: 978-3-95450-230-1 ISSN: 2673-5350 doi:10.18429/JACoW-IBIC2021-TUOA01

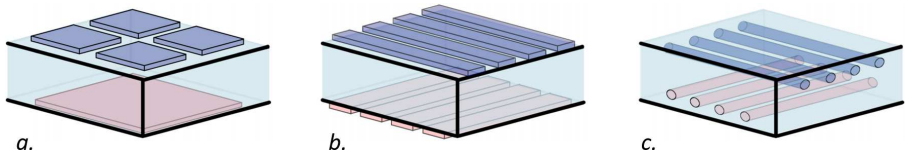

Figure 2: A sketch (not to scale) illustrating different detector electrode designs that are currently in use (*a*, *b*), and the electrode design presented in this paper (*c*). This figure is reproduced from [17].

X-ray transmission of scCVD diamond is presented alongside that of other common detector materials in Fig. 1, using data compiled from [10]. Diamond has superior transmissivity, and no absorption edges around common synchrotron experimental photon energies, 4 - 20 keV. Also included for comparison are the transmission of common fluorescent screen materials that a beamline may use to monitor the beam profile.

The ionizing radiation that is absorbed in the detector material generates electron-hole pairs. Under the influence of an electrical bias the electrons and holes migrate towards the external electrodes. An arrangement of four 'quadrant' electrodes can provide a position measurement in two dimensions, as depicted in Fig. 2 *a*. This design originated in the late 1990s using polycrystalline diamond [11], and was then improved upon through the use of single-crystal diamond [12]. Single-crystal diamond detectors are now available 'off the shelf' from multiple commercial suppliers. Such commercially available devices have the ability to provide 2-dimensional beam position measurements with precision at nanometer scales [13, 14]. However, this common design of instrument makes a number of trade-offs to obtain such precise 2-dimensional beam position measurements.

The first trade-off is the small position-sensitive region of the detector. Only when the X-ray beam footprint straddles two quadrants is a position measurement possible. When the incident X-ray beam falls wholly within one quadrant the instrument cannot provide an accurate position measurement. It can only be inferred that the beam is located *somewhere* within that one quadrant. The position of a 100 µm wide X-ray beam can only be accurately measured if it passes through the instrument within ± 100 µm of the quadrant gap.

The second trade-off is that since the position measurement for the smallest beamsizes can be limited by the gap between the quadrants, there is a strong motivation to make this isolating gap between the surface electrodes as small as possible, typically 2 - 5 µm [14]. This leads to delicate instruments with very small isolating gaps where surface contaminants, debris, or damage can easily 'short' two neighbouring electrodes and impair position measurement.

The third trade-off is the inability to obtain X-ray beam profile information. With only four pixels, or 'quadrants', the beam measurement is limited to a simple X- and Y-position. To tackle this third problem in particular, an approach using 'strip-electrodes' applied to the surface of the diamond has been developed, enabling beam profile information to be measured [15, 16]. A sketch illustrating this electrode configuration is depicted in Fig. 2 *b*. However, each additional electrode introduces another potential source of detector failure should an electrical short occur.

A new design of transparent X-ray diagnostic is presented in these proceedings. This detector aims to address the three drawbacks listed above. This detector utilises buried graphitic electrodes instead of surface strip-electrodes, as is illustrated in Fig. 2 *c*. The instrument has been successfully tested at Diamond Light Source, and is cable of transmissively measuring the beam profile in real time [17].

LASER-WRITING OF DIAMOND

The detector presented here makes use of recent developments in adaptive optics to laser-write graphitic tracks buried within bulk diamond. These are fabricated using an ultrashort pulse laser technique. At the laser focal point there is sufficient energy deposited into the diamond that a local phase transition can take place: electrically non-conductive diamond is converted into conductive graphite. In this section, a short history of the use of graphitic electrodes will be presented.

The technique was first demonstrated in the late 1990s as a method of electrically contacting doped layers within CVD grown diamond, using graphite columns that extended to the surface of the diamond [18]. Later work produced '3D diamond detectors' for ionizing radiation, with columnar graphitic electrodes embedded within the bulk diamond [19]. A square array of electrodes was written through the diamond plate at 200 µm intervals. Half of the columns were connected to the 'bias' supply and half of the columns were connected to the 'measurement' circuit. This 'interdigitated' electrode approach had a number of advantages over traditional top-and-bottom surface electrodes for radiation detectors: firstly it was shown to increase the radiation resistance of detectors to high energy particles; secondly the array of graphitic 'micro-channels' reduced the mean distance between electrodes, enabling greater charge collection efficiency. A useful summary of the first results obtained for particle tracking detectors is provided by [20].

The second half of the 2010s has seen further research into the use of scCVD diamond particle detectors with graphitic columns as electrodes: measurements of different charged particle beams [21, 22]; studying the effects of different hexagonal vs cubic column arrays [23]; modelling such detectors [24]; investigating the graphetization processes [25]; and investigating the effect that columnar electrodes have on the diamond stress and charge transport properties [26]. All of these papers are related to detector work for LHC

ISBN: 978-3-95450-230-1 ISSN: 2673-5350 doi:10.18429/JACoW-IBIC2021-TUOA01

and similar machines for particle tracking, where radiation tolerant diamond detectors are essential given the extremely high dose rates experienced.

As well as simple columnar electrodes, improvements in adaptive optics have enabled the writing of graphitic wires following arbitrary 3D paths within a diamond plate [27], or long electrodes running parallel to the surface of the plate [28]. The listed papers are not an exhaustive list of the research in this field, but are intended to give the reader a flavour of the work being carried out.

Buried graphitic electrodes provide protection from mechanical and chemical damage, and from conductive surface contaminants. Graphite is more transmissive to X-rays than an equivalent thickness of aluminium, titanium, or other traditional electrode material. Additionally, there is no danger of the electrode material introducing new absorption edges that may affect synchrotron experiments, as the K-edge in both graphite and diamond (carbon sp^2 and sp^3 respectively) differ by just a few eV [29].

X-RAY IMAGING MONITOR DESIGN

The detector design utilised in this work was first presented in [30]. The diamond plate was provided by *Element Six* for the purposes of this research and is described by the supplier as 'Single Crystal Optical Plus' grade material.

Figure 3 presents the layout of the detector. Two sets of 11 parallel 'bias' electrodes run under the surface of the diamond plate, orthogonal to two sets of 11 parallel 'measurement' electrodes. To identify the wires, the shorter of the sets of wires are referred as the 'X' electrodes, and the longer set of wires will be referred to as the 'Y' electrodes. This naming convention arose because in the experimental testing the 'X' wires were oriented horizontally and the 'Y' wires were oriented vertically.

The 'X' electrodes are located at a depth of 200 µm within the material, and the 'Y' electrodes are located at a depth of 100 µm, providing an electrode separation of 100 µm within the diamond. There is an in-plane spacing of 50 µm between each individual electrode within each array. Each electrode comprises of three parallel tracks laterally spaced by 2 µm.

The electrodes are connected to the surface by vertical graphitic columns referred to as 'vias'. These are located at the edges of the diamond plate for the purpose of connecting the buried electrodes to a surface metallisation pad, well away from the centre of the detector where the beam would pass through.

The electrodes each comprise of three parallel tracks to improve conductivity, as can be observed in Fig. 4 A. The resistance of each of the buried graphitic electrodes was measured to be $31 \pm 6\,\mathrm{k\Omega}\,/\,\mathrm{mm}$.

The repetition of two arrays of 11 'X' electrodes and two arrays of 'Y' electrodes is to provide multiple potential 11 x 11-pixel imaging regions, each with a pixel pitch of 50 x 50 µm. This redundancy was built into the detector in case of a graphitic track or a surface contact being incomplete or non-conductive. Arrays of 11 x 11 pixels were

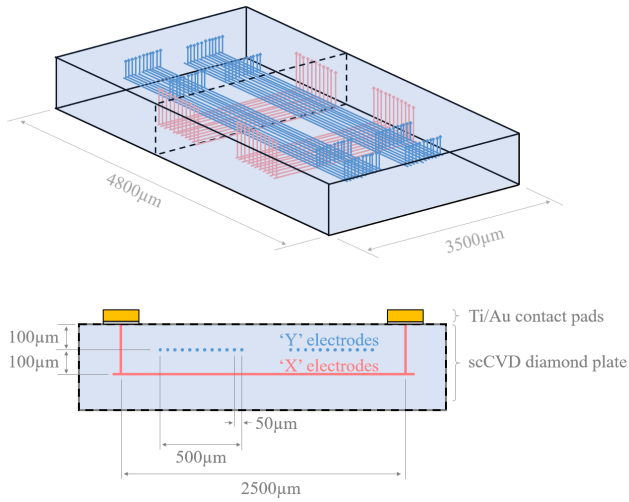

Figure 3: Top: A sketch (not to scale) of the wire layout within the diamond plate. A black dotted line indicates the region of the cross section presented. Bottom: The cross-section through the diamond plate. The location of the surface metallisation at the edge of the detector is shown. This figure is reproduced from [30].

chosen as this matched the number of signal acquisition hardware channels that were available to the authors at the time of this detector's design.

The overall 0.6 mm thickness of the diamond plate was dictated only by the availability of material. The relatively large 100 µm separation between the 'X' and 'Y' electrodes within this prototype detector was chosen to increase X-ray absorption and charge carrier generation. The 100 µm separation between the surface of the diamond plate and the upper electrode array was arbitrarily chosen, and for a future detector could be ~ 5 µm.

Ideally, a transmissive detector would remain as thin as practical so as to minimise X-ray absorption. These relatively large inter-electrode spacing and large electrode-to-surface spacing was chosen only so as to ensure comfortable margin for any alignment errors that may have occurred during fabrication of this first prototype.

The design ensures that there is no surface metallisation, or indeed any surface features, present within the active region of the detector. The upward vias used to extract the signal are located at the edges of the diamond plate, at least 500 µm away from the centre of the interaction points.

EXPERIMENTAL RESULTS

To test the response of the detector to incident X-rays, it was installed in air at the sample point of the I18 beamline at Diamond Light Source [31]. The beamline was configured to deliver a collimated flux of up to 3×10^{11} ph / s at a tunable photon energy. The beam size at the detector could be altered from 20 µm up to 250 µm FWHM.

Also mounted along the beam path was an an ion chamber (beam intensity monitor), a traditional four-quadrant X-ray

ISBN: 978-3-95450-230-1 ISSN: 2673-5350 doi:10.18429/JACoW-IBIC2021-TUOA01

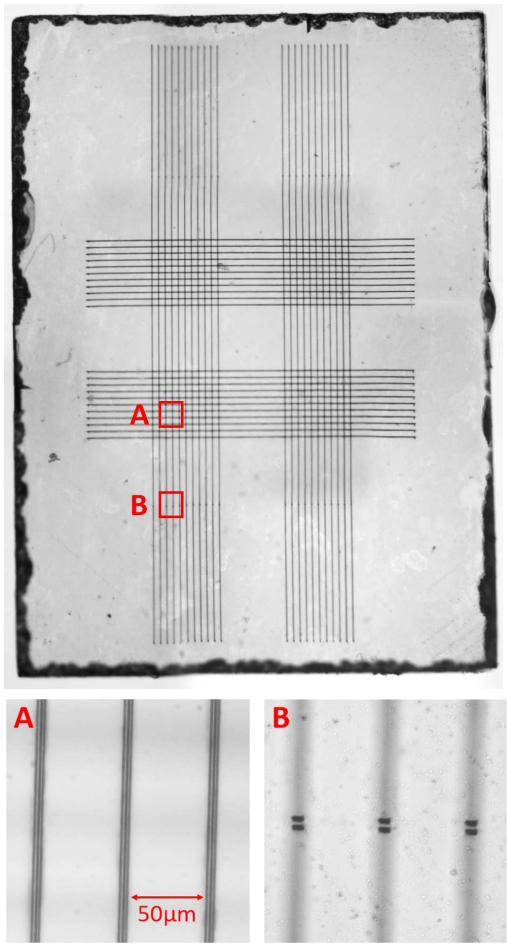

Figure 4: Top: A microscope image of the diamond plate showing the fabricated graphitic wires. Bottom left: A magnified view of the area shown in the red square marked 'A'. The upper electrodes can be seen in focus; the lower electrodes are out of the microscope focus. Bottom right: A magnified view of the area shown in the red square marked 'B'. The upwards 'vias' are visible in focus. This figure is reproduced from [17].

beam position monitor (XBPM)[1], and a CMOS camera system monitoring a cerium-doped lutetium-aluminium-garnet, LuAG:Ce, fluorescent screen. These were for the purposes of monitoring the incident beam with commonly used beamline instrumentation, so that the performance of this graphitic wire detector could be quantitatively compared. This apparatus was mounted together onto a support plate, and the whole assembly was bolted onto the a motorised X, Y stepper motor stage so that the detectors could be aligned to the beam path. A sketch showing the experimental set up at the I18 sample-point is presented in Fig. 5.

1-Dimensional Profile Measurements

A 1-dimensional beam profile can be obtained by applying a constant bias to each of the 11 measurement channels. With the beam centred upon one of the four imaging regions,

[1] A *Sydor Technologies* diamond beam position monitor (DBPM).

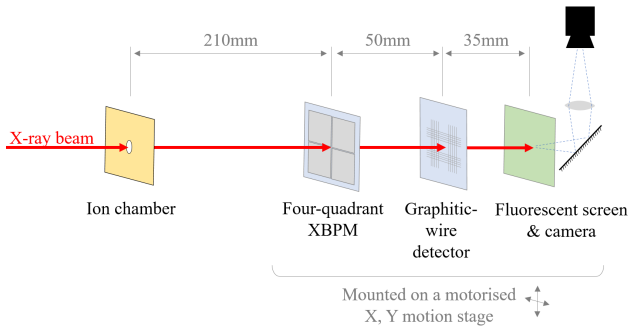

Figure 5: A sketch showing the layout of the detectors along the X-ray beam path.

a static bias of + 10 V was applied to all of the corresponding 'X' electrodes. Each 'Y' electrode was connected to a low-impedance electrometer which was used to record the resulting signal currents. The magnitude of the resulting signal currents is directly proportional to the absorbed photon power, providing a 1-dimensional profile of the X-ray beam. A comparison of the vertical X-ray beam profile measured by the detector and that obtained by the fluorescent screen and CMOS camera is presented in Fig. 6. This figure shows two examples of different beamsizes: 180 µm FWHM beam size (top), and 22 µm (bottom). The measurements of the X-ray beam profile using the graphitic wire detector show good agreement with that obtained from the camera. However, it is noted that the spatial resolution of the graphitic wire detector (the 'spread function') is limited to the 50 µm pixel pitch, and it cannot resolve the narrow, 22 µm beam profile.

Imaging Results

Readout of the individual pixels was achieved using a novel lock-in modulation technique. Rather than apply a static 'DC' bias to an individual electrode or to a set of electrodes, a modulated 'AC' bias was used. A different frequency was applied to each of the 11 'X' electrodes (1.1 kHz, 1.2 kHz, 1.3 kHz, ..., etc), with a modulation amplitude of 0.5 V around a DC level of 0 V.

The resulting signal currents were acquired at 20 kHz from the perpendicular electrodes with low impedance electrometers. A Fourier transform of the signal currents from each measurement electrode is carried out. The Fourier amplitude of the measured signal at a given frequency is proportional to the flux passing through the detector at the intersection between the measurement electrode and the bias electrode modulated by that frequency. An illustration of this approach is presented in Fig. 7.

Shown in Fig. 8 are an example of the 20 kHz measured signal currents obtained, shown in the time domain (top), and in the frequency domain (bottom). This acquisition frequency and modulation frequencies have been specifically chosen such that when acquiring a 10 ms acquisition (i.e. 100 FPS capture rate) each bin of the Fourier transform

ISBN: 978-3-95450-230-1 ISSN: 2673-5350 doi:10.18429/JACoW-IBIC2021-TUOA01

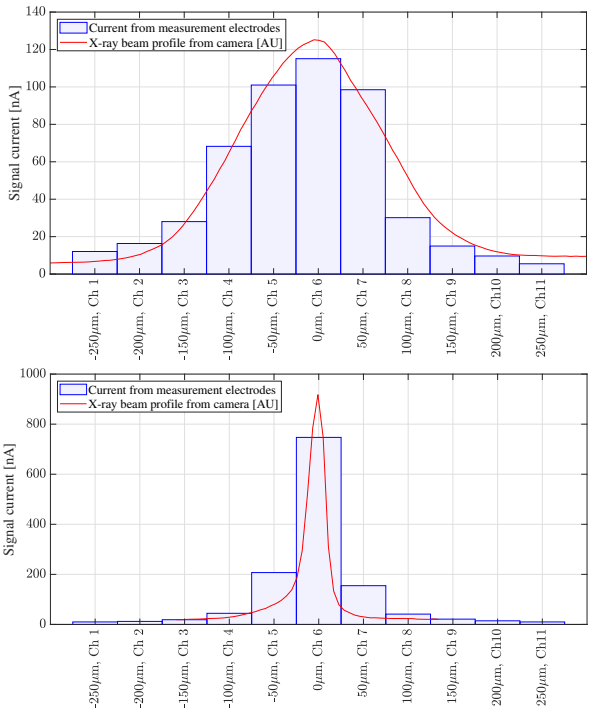

Figure 6: Vertical 1-dimensional beam profile measurements obtained using a static bias, compared to fluorescent screen camera image profiles. Top: 180 µm FWHM beam size. Bottom: 22 µm FWHM beam size.

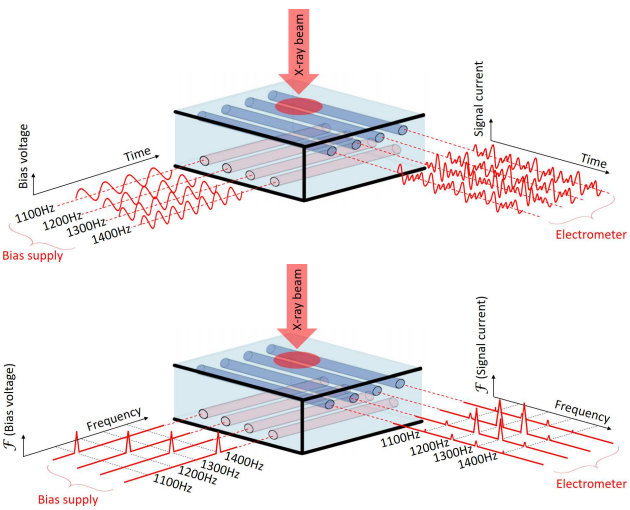

Figure 7: The readout scheme presented in this work utilises a different modulation frequency applied to each bias electrode. The individual modulation frequencies are detectable at the measurement electrodes. Top: A time-domain view of the modulation scheme. Bottom: A frequency-domain picture, showing how the individual modulation frequencies measured by the electrometer build up a picture of the beam profile upon the detector. This figure is reproduced from [17].

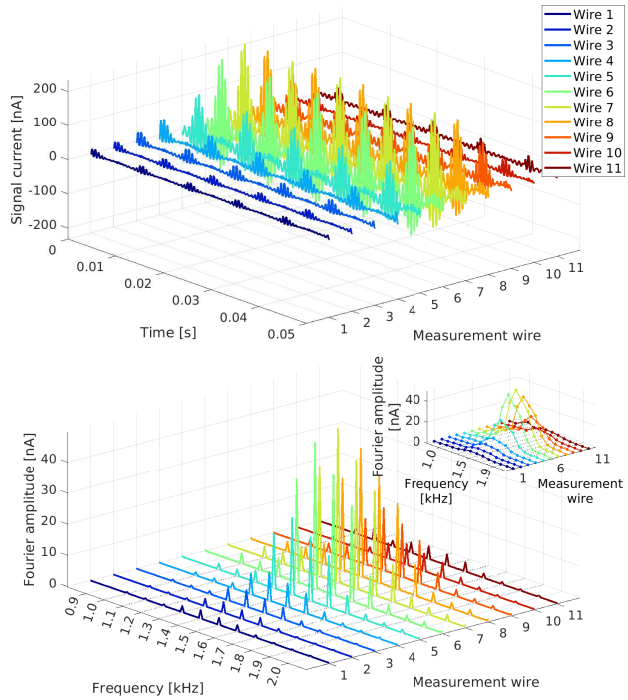

Figure 8: Top: The 20 kHz signals acquired from 11 measurement electrodes whilst the X-ray beam is illuminating the detector. Bottom: The Fourier transform of a 1 second long acquisition at 20 kHz signals. Inset: The Fourier transform of a 10 ms acquisition. These currents correspond to the leftmost image from Fig. 9.

corresponds to one modulation frequency, and thus one column of pixels on the detector.

Figure 9 presents the imaging results obtained during a scan of the beamline's mirror curvature, bringing the beam into focus at the location of the sample-point over the course of the sequence of images. The X-ray beam is focused from 180 µm down to 40 µm FWHM (from left to right). Each image shows a region 500 x 500 µm.

To determine the position-sensitivity of the detector, the beam profile was recorded as the instrument was stepped vertically through the X-ray beam. A 180 µm FWHM X-ray beam with an approximately Gaussian profile was used for these tests. At each position of the scan images were acquired at 100 FPS. A 2-dimensional Gaussian fitting routine is applied to the image to obtain the centroid position. Figure 10 presents the results of these scans. The error bars are the standard deviation in fitted beam position from the sequential detector images acquired at each scan position. They represent the uncertainty on the acquired beam position for the 180 µm FWHM X-ray beam, and provide an upper-bound on the beam position resolution. The mean standard deviation in position measurement was 600 nm, or 0.3 % of the vertical beam size, FWHM.

To determine the signal linearity that can be obtained while using this lock-in modulation acquisition method, a scan of beam intensity was carried out using a series of adjustable attenuation filters. These can be inserted into the

ISBN: 978-3-95450-230-1 ISSN: 2673-5350 doi:10.18429/JACoW-IBIC2021-TUOA01

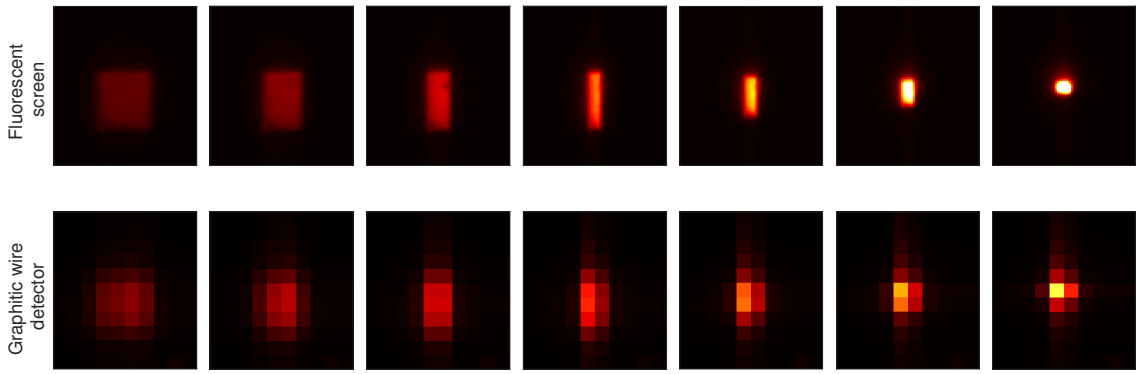

Figure 9: Images obtained during beam focusing from the fluorescent screen (top) and from the graphitic wire detector (bottom). In both cases the image size is 500 x 500 µm.

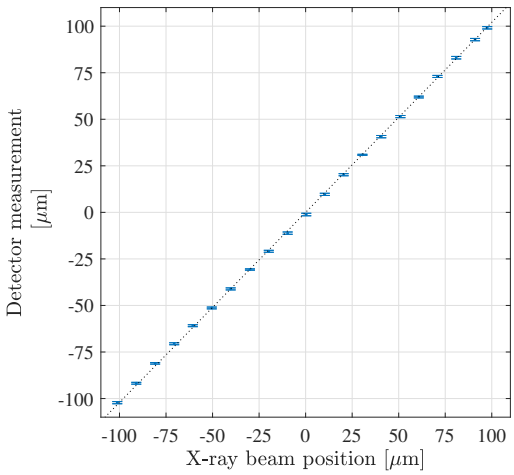

Figure 10: The detector is scanned across the incident X-ray beam in steps of 10 µm. At each point in the scan images are acquired at 100 FPS.

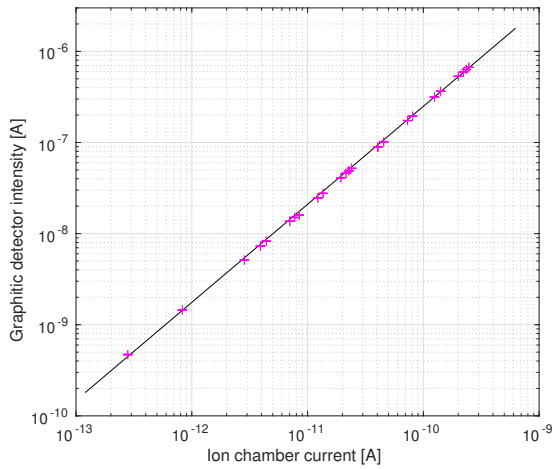

Figure 11: The signal linearity from the graphitic wire XBPM is plotted against that measured using the beamline's intensity monitor diode.

beam path to reduce the sample-point flux. The beamline's ion-chamber was used as the flux reference measurement. The output of the ion chamber is directly proportional to the absorbed power, which for a fixed photon energy is directly proportional to the incident flux.

The beam intensity measured by the graphitic wire detector was obtained by taking the sum of all pixels in the acquired image, i.e. the sum of the Fourier transform amplitudes. Figure 11 presents this intensity measurement as the incident flux is varied over 3-orders of magnitude. These results demonstrate that the signal linearity of the graphitic wire XBPM is at least as good as the beamline's ion chamber over 3-orders of magnitude of flux.

CHARGE CARRIER MODELLING

To help optimise the detector performance and evaluate different electrode geometries for future detectors, a simple model of carrier motion through the diamond plate has been produced. This section describes the carrier dynamics used in the model. This work is expanding upon similar modelling of silicon detectors carried out in [32], where Chapter 7 in particular contains useful information and equations to describe the motion of carriers through a crystal.

At room temperature, liberated charge carriers in diamond will diffuse randomly in space because of thermal energy. This is analogous to Brownian motion, and is modelled by the Wiener process. In this model individual atomistic effects are neglected, and only 'microscopic' net motions are be considered. The overall probability of finding a particle at location x after time t, given starting conditions of $x_0 = 0$ and $t_0 = 0$, is a Gaussian distribution given by Eq. (1):

$$p(t,x) = \frac{1}{\sqrt{4\pi D(t-t_0)}} \exp\left(-\frac{(x-x_0)^2}{4D(t-t_0)}\right) \quad (1)$$

The constant D is the Einstein diffusion coefficient:

$$D = \frac{\mu_q k_B T}{q} \quad (2)$$

ISBN: 978-3-95450-230-1 ISSN: 2673-5350 doi:10.18429/JACoW-IBIC2021-TUOA01

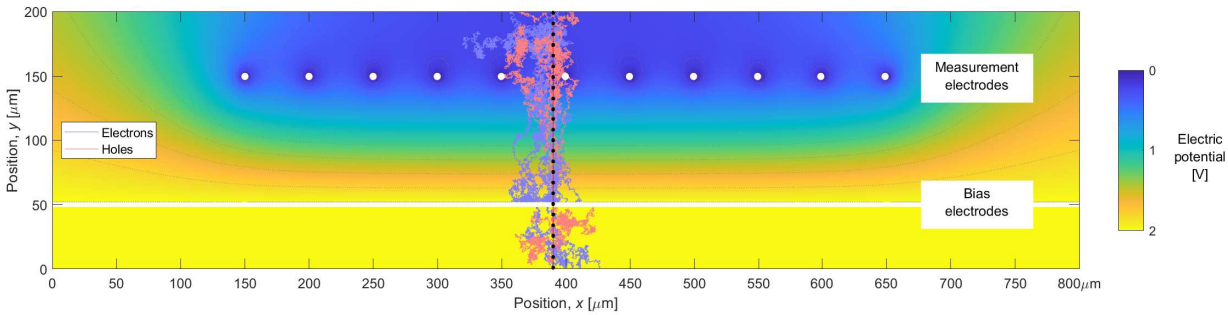

Figure 12: Simulated trajectories of 25 generated electron-hole pairs through a 800 x 200μm cross-section of detector. The electron-hole origins are marked by black dots along the path of the incident beam of ionizing radiation.

where μ_q is the mobility of the charge carrier; k_B is the Boltzmann constant; T is the absolute temperature; and q is the electrical charge of the particle.

In addition to the random diffusion of carriers they may also undergo a net drift under the influence of an external electric field. Their drift velocity is dependent on the electric field applied across the material. At high fields the velocity becomes limited due to collisions with atoms in the crystal lattice and energy loss through the generation of phonons. The resulting net carrier velocities, $\vec{v_q}$, are given by Eq. (3):

$$\vec{v_q} = \frac{\mu_q \vec{E}}{1 + \frac{\mu_q \vec{E}}{v_{q,s}}} \tag{3}$$

where $\vec{E}$ is the electric field strength; and $v_{q,s}$ is the saturation velocity of the charge carriers within the diamond.

The mean drift distances travelled by a carrier, $\vec{x_q}$, in a given time interval, t, is simply the carrier velocity multiplied by the time interval:

$$\vec{x_q}(t) = \vec{v_q}\, t \tag{4}$$

Using published values for the carrier mobilities, lifetimes, and saturation velocities typically found similar synthetic diamond plates [33], Eqs. (1) and (4) can be used to model the position of carriers after discrete time steps. The simulation uses time steps of 5 ps. This is a sufficiently large time step that quantum and atomistic effects can be neglected, but small enough to accurately reflect the motion of charge carriers through detector regions on micrometer scales. The carrier trajectories are modelled until either they reach an electrode or the carrier lifetime is reached. An example of this modelling is presented in Fig. 12.

Future work will concentrate on confirming the validity of this model by comparing it to experimental data. Comparison of the modelled charge collection efficiency and experimental data is useful in determining the quality of the diamond plates used for detectors, as dislocations and impurities affect the carrier dynamics [34, 35]. Accurate modelling of the lateral drift of charge carriers will allow limitations on the ultimate spatial resolution of the detector to be established.

CONCLUSIONS

The pixel detector presented in this work is demonstrated to be capable of transmissively imaging the synchrotron X-ray beam profile. A modulation lock-in readout technique has been developed which enables all pixels to be read simultaneously. Images of the beam profile can be obtained at up to 100 FPS.

Beam motions much smaller than the 'pixel size' can be easily resolved by applying 2D Gaussian fitting to determine the centroid, and the resolution of the position measurement is 600 nm for 10 ms acquisitions and 180 μm beam size FWHM. Intensity linearity is equivalent to a standard ion-chamber over 3-orders of magnitude of flux.

Ongoing modelling is being used to help optimise future detector design and electrode geometry, and probe possible constraints on spatial resolution of the detector due to lateral charge diffusion.

The single crystal diamond detector includes no metallisation in the beam path and introduces fewer absorption edges that may interfere with beamline experiments. Keeping the transmissive region of the sensor free from metallisation also reduces the danger of electrodes being damaged by high incident flux. The detector may be permanently installed in the X-ray beam path, offering significant advantages over fluorescent screens, or knife-edge scans which intercept a significant portion of the synchrotron flux or block it entirely.

ACKNOWLEDGEMENTS

The authors wish to acknowledge the support of many individuals and groups that aided in this research. The scCVD diamond plate used to create this detector was provided by Element Six. We wish to acknowledge the contributions of Patrick Salter for the graphitic electrode fabrication, at the University of Oxford. Ben Green carried out the metallisation, Frank Courtney carried out the wire bonding, and Yorck Ramachers provided useful input on charge carrier modelling, all at the University of Warwick. The X-ray measurements were conducted on the I18 beamline at Diamond Light Source, and we thank the I18 staff for their assistance. Finally, we wish to acknowledge the support of Guenther Rehm for his contributions to the project.

ISBN: 978-3-95450-230-1 ISSN: 2673-5350 doi:10.18429/JACoW-IBIC2021-TUOA01

REFERENCES

[1] G. Ice *et al.*, "The Race to X-ray Microbeam and Nanobeam Science", *Science*, vol. 334, pp. 1234–1239, 2011. doi:10.1126/science.1202366

[2] J. Mosselmans *et al.*, "A time resolved microfocus XEOL facility at the Diamond Light Source", *Journal of Physics: Conference Series*, vol. 425, p. 182009, 2013. doi:10.1088/1742-6596/425/18/182009

[3] C. A. Murray *et al.*, "New Synchrotron Powder Diffraction Facility for Long Duration Experiments", *Applied Crystallography*, vol. 50, pp. 172–183, 2017. doi:10.1107/S1600576716019750

[4] B. Hettel, "Beam stability at light sources", *Review of Scientific Instruments*, vol. 73, pp. 1396–1401, 2002. doi:10.1063/1.1435812

[5] G. Decker, "Beam Stability in Synchrotron Light Sources", in *Proc. DIPAC'05*, Lyon, France, pp. 233–237, 2005.

[6] C. Steier, "Beam Stability Requirements for 4th Generation Synchrotron Light Sources Based on MBA Lattices", 1st BES Light Sources Beam Stability Workshop, 2018.

[7] S. Alcock *et al.*, "High-speed adaptive optics using bimorph deformable X-ray mirrors", *Review of Scientific Instruments*, vol. 90, p. 021712, 2019. doi:10.1063/1.5060737

[8] H. Mimura *et al.*, "Breaking the 10 nm barrier in hard-X-ray focusing", *Nature Physics*, vol. 6, pp. 122–125, 2010. doi:10.1038/NPHYS1457

[9] E. Abruna *et al.*, "Real-time feedback for X-ray adaptive optics with an interferometric absolute distance sensor array", *Proceedings of SPIE: Adaptive X-Ray Optics V*, vol. 10761, p. 107610H, 2018. doi:10.1117/12.2323698

[10] B. L. Henke *et al.*, "X-ray interactions: photoabsorption, scattering, transmission, and reflection at E=50-30000 eV, Z=1-92", *Atomic Data and Nuclear Data Tables*, vol. 54, pp. 181–342, 1993. doi:10.1006/adnd.1993.1013

[11] P. Bergonzo *et al.*, "Diamond-based semi-transparent beam-position monitor for synchrotron radiation applications", *Journal of Synchrotron Radiation*, vol. 6, pp. 1–5, 1999. doi:10.1107/s090904959801509x

[12] J. Morse *et al.*, "Single crystal CVD diamond as an X-ray beam monitor", *Diamond and Related Materials*, vol. 16, pp. 1049–1052, 2007. doi:10.1016/j.diamond.2006.11.081

[13] C. Bloomer *et al.*, "The use of single-crystal CVD diamond X-ray beam diagnostics for synchrotron beamline commissioning and operation at Diamond Light Source Ltd", *IEEE Nuclear Science Symposium Conference Record*, 2016. doi:10.1109/NSSMIC.2016.8069893

[14] E. Griesmayer *et al.*, "Applications of single-crystal CVD diamond XBPM detectors with nanometre X-ray beams", *AIP Conference Proceedings*, vol. 2054, p. 060052, 2019. doi:10.1063/1.5084683

[15] D. Shu *et al.*, "CVD-Diamond-Based Position Sensitive Photoconductive Detector for High-Flux X-Rays and Gamma Rays", in *Proc. PAC'99*, New York, USA, pp. 2090–2092, 1999. doi:10.1109/PAC.1999.794382

[16] T. Zhou *et al.*, "Pixelated transmission-mode diamond X-ray detector", *Journal of Synchrotron Radiation*, vol. 22, pp. 1396–1402, 2015. doi:10.1107/S1600577515014824

[17] C. Bloomer *et al.*, "A single-crystal diamond X-ray pixel detector with embedded graphitic electrodes", *Journal of Synchrotron Radiation*, vol. 27, pp. 599–607, 2016. doi:10.1107/s160057752000140x

[18] R. Walker *et al.*, "Formation of buried p-type conducting layers in diamond", *Applied Physics Letters*, vol. 71, pp. 1492–1494, 1997. doi:10.1063/1.119946

[19] A. Oh *et al.*, "A novel detector with graphitic electrodes in CVD diamond", *Diamond and Related Materials*, vol. 38, pp. 9–13, 2013. doi:10.1016/j.diamond.2013.06.003

[20] F. Bachmair *et al.*, "A 3D diamond detector for particle tracking", *Nuclear Instruments and Methods in Physics Research, Section A*, vol. 786, pp. 97–104, 2015. doi:10.1016/j.nima.2015.03.033

[21] G. Forcolin *et al.*, "Study of a 3D diamond detector with photon and proton micro-beams", *Diamond and Related Materials*, vol. 65, pp. 75–82, 2016. doi:10.1016/j.diamond.2016.02.005

[22] M. Girolami *et al.*, "Investigation with β-particles and protons of buried graphite pillars in single-crystal CVD diamond", *Diamond and Related Materials*, vol. 84, pp. 1–10, 2018. doi:10.1016/j.diamond.2018.02.014

[23] M. J. Booth *et al.*, "Study of cubic and hexagonal cell geometries of a 3D diamond detector with a proton micro-beam", *Diamond and Related Materials*, vol. 77, pp. 137–145, 2017. doi:10.1016/j.diamond.2017.06.014

[24] G. Forcolin *et al.*, "Simulation of 3D diamond detectors", *Nuclear Instruments and Methods in Physics Research, Section A*, vol. 845, pp. 72–75, 2017. doi:10.1016/j.nima.2016.06.099

[25] T. Lühmann *et al.*, "Investigation of the graphitization process of ion-beam irradiated diamond using ellipsometry, Raman spectroscopy and electrical transport measurements", *Carbon*, vol. 121, pp. 512–517, 2017. doi:10.1016/j.carbon.2017.05.093

[26] S. Salvatori *et al.*, "Diamond Detector with Laser-Formed Buried Graphitic Electrodes: Micron-Scale Mapping of Stress and Charge Collection Efficiency", *IEEE Sensors Journal*, vol. 19, pp. 11908–11917, 2019. doi:10.1109/JSEN.2019.2939618

[27] B. Sun *et al.*, "High conductivity micro-wires in diamond following arbitrary paths", *Applied Physics Letters*, vol. 105, p. 231105, 2014. doi:10.1063/1.4902998

[28] A. Khomich *et al.*, "Very long laser-induced graphitic pillars buried in single-crystal CVD-diamond for 3D detectors realization", *Diamond and Related Materials*, vol. 90, pp. 84–92, 2018. doi:10.1016/j.diamond.2018.10.006

[29] A. Hamon *et al.*, "ELNES study of carbon K-edge spectra of plasma deposited carbon films", *Journal of Materials Chemistry*, vol. 14, pp. 2030–2035, 2004. doi:10.1039/b406468m

[30] C. Bloomer *et al.*, "A Single Crystal CVD Diamond X-ray Beam Diagnostic with Embedded Graphitic Wire Electrodes", *Proceedings of the 13th International Conference on Synchrotron Radiation Instrumentation*, vol. 2054 p. 060058, 2018. doi:10.1063/1.5084689

ISBN: 978-3-95450-230-1 ISSN: 2673-5350 doi:10.18429/JACoW-IBIC2021-TUOA01

[31] J. Mosselmans *et al.*, "I18 - the microfocus spectroscopy beamline at the Diamond Light Source", *Journal of Synchrotron Radiation*, vol. 16, pp. 818–824, 2009. doi:10.1107/S0909049509032282

[32] J. Becker, "Signal development in silicon sensors used for radiation detection", PhD Dissertation zur Erlangung des Doktorgrades des Department Physik der Universitat Hamburg, Germany, 2010.

[33] M. Pomorski *et al.*, "Charge transport properties of single crystal CVD-diamond particle detectors", *Diamond and Related Materials*, vol. 16, pp. 1066–1069, 2007. doi:10.1016/j.diamond.2006.11.016

[34] A. Lohstroh *et al.*, "Effect of dislocations on charge carrier mobility–lifetime product in synthetic single crystal diamond", *Applied Physics Letters*, vol. 90, p. 102111, 2007. doi:10.1063/1.2711754

[35] A. Tarun *et al.*, "Impact of impurities and crystal defects on the performance of CVD diamond detectors", *Diamond and Related Materials*, vol. 63, pp. 169–174, 2016. doi:10.1016/j.diamond.2015.08.018